

# The correlation between the average density of circumnuclear molecular gas and AGN activity for massive elliptical galaxies

Yutaka FUJITA<sup>1</sup>, Takuma IZUMI<sup>2</sup>, Nozomu KAWAKATU<sup>3</sup>, Hiroshi NAGAI<sup>2,4</sup>,  
Ryo HIRASAWA,<sup>1</sup> and Yu IKEDA<sup>1</sup>

<sup>1</sup>Department of Physics, Graduate School of Science Tokyo Metropolitan University 1-1  
Minami-Osawa, Hachioji-shi, Tokyo 192-0397

<sup>2</sup>National Astronomical Observatory of Japan, 2-21-1 Osawa, Mitaka, Tokyo 181-8588

<sup>3</sup>National Institute of Technology, Kure College, 2-2-11, Agaminami, Kure, Hiroshima,  
737-8506, Japan

<sup>4</sup>The Graduate University for Advanced Studies, SOKENDAI, Osawa 2-21-1, Mitaka, Tokyo  
181-8588

\*E-mail: y-fujita@tmu.ac.jp

Received 2099 January 1; Accepted 2099 January 1

## Abstract

Massive molecular clouds have been discovered in massive elliptical galaxies at the center of galaxy clusters. Some of this cold gas is expected to flow in the central supermassive black holes and activate galactic nucleus (AGN) feedback. In this study, we analyze archival ALMA data of 9 massive elliptical galaxies, focusing on CO line emissions, to explore the circumnuclear gas. We show that the mass of the molecular gas within a fixed radius (500 pc) from the AGNs ( $M_{\text{mol}} \sim 10^7\text{--}10^8 M_{\odot}$ ) is correlated with the jet power estimated from X-ray cavities ( $P_{\text{cav}} \sim 10^{42}\text{--}10^{45} \text{ erg s}^{-1}$ ). More specifically, the power is proportional to the average density of the circumnuclear gas. The mass accretion rate of the circumnuclear gas  $\dot{M}$  also has a correlation with  $P_{\text{cav}}$ . On the other hand, the continuum luminosities at  $\sim 1.4$  GHz and  $\sim 100\text{--}300$  GHz have no correlation with  $M_{\text{mol}}$ . These results indicate that the circumnuclear gas is sustaining the long-term AGN activities ( $\sim 10^7$  yr) rather than the current ones. We also study the origin of the continuum emission from the AGNs at  $\sim 100\text{--}300$  GHz and find that it is mostly synchrotron radiation. For low-luminosity AGNs, however, dust emission appears to contaminate the continuum.

**Key words:** galaxies: active — galaxies: elliptical and lenticular, cD — galaxies: ISM — galaxies: jets — galaxies: nuclei

## 1 Introduction

Massive elliptical galaxies are often located at the center of galaxy clusters. They host supermassive black holes, which are observed as active galactic nuclei (AGNs). While the cooling time of the hot gas in the galaxies is much smaller ( $\lesssim 10^8$  yr) than the age of the Universe (Fabian 1994), the

AGNs are expected to serve as heating sources and prevent the development of massive cooling flows (AGN feedback; Churazov et al. 2000; McNamara & Nulsen 2007; Fabian 2012). Since the galaxies are immersed in the hot gas, it may be natural to assume that the hot gas feeds into the black holes in the form of the Bondi accretion (Bondi 1952) and stimulates the AGNs. In fact, Allen et al. (2006)

found a tight correlation between the Bondi accretion rates and the power emerging from the AGNs in relativistic jets. However, later studies have revealed that the correlation is weak (Russell et al. 2013).

In addition to the hot gas, cold molecular gas has been discovered in the massive elliptical galaxies (e.g. Edge 2001; Salomé & Combes 2003; David et al. 2014; McNamara et al. 2014). It has been indicated that nebular emission, enhanced star formation, and AGN activities are recognized when the entropy of the hot gas decreases to  $\lesssim 30 \text{ keV cm}^2$ , or almost equivalently when the radiative cooling time is  $\lesssim 1 \text{ Gyr}$  (e.g. Cavagnolo et al. 2008; Rafferty et al. 2008; Sanderson et al. 2009; Main et al. 2017). This suggests that the hot gas turns into cold gas through radiative cooling and the cold gas induces the star formation and the AGN activities. Recently, Fujita et al. (2022) discussed gas circulation in the massive elliptical galaxies using a semi-analytical model. They indicated that while some of the cold gas is consumed in star formation, the rest flows into the galactic center. Moreover, if a circumnuclear disk is formed around the central black hole, disk instabilities regulate the gas accretion toward the black hole; the overall AGN activity depends on the mass of the disk.

In this paper, we analyze Atacama Large Millimeter Array (ALMA) archival data of the galaxies and seek correlations among the properties of circumnuclear molecular gas and the AGN activity, which may support the idea that the gas fuels the AGNs. We note that Russell et al. (2019) have compared the mass of the circumnuclear molecular gas with the AGN jet power and found a correlation (their Figure 7). However, they measured the mass in a single ALMA synthesized beam centered on the AGNs. Since the physical size of a given beam is larger for more distant objects, the mass inside it tends to be larger, while distant AGNs are observationally biased toward brighter and powerful ones. This could create an artificial correlation. To lessen such biases, we focus on the mass within a fixed physical radius. We also study the mass accretion rates and the radio continuum luminosities of the AGNs to further investigate the fueling process. We assume  $H_0 = 70 \text{ km s}^{-1} \text{ Mpc}^{-1}$ ,  $\Omega_m = 0.3$ , and  $\Omega_\Lambda = 0.7$  in this study. All errors are  $1\sigma$  unless otherwise noted.

## 2 Data Reduction

We analyzed archival ALMA observations of CO line emissions from the cold gas in massive elliptical galaxies at the center of galaxy clusters, and we investigated relations between the cold gas and the AGN activity. Targets were selected from those studied in Olivares et al. (2019) and Russell et al. (2019). From the sample, we chose the

ones for which AGN jet powers ( $P_{\text{cav}}$ ) have been estimated through observations of X-ray cavities. Moreover, we chose those for which the inner 500 pc (1 kpc in diameter) is resolved with ALMA. The selected sample includes M87 and RXJ0821+0752. However, the molecular gas detected in M87 is located in the outer region of the galaxy and has no connection to the AGN (Simionescu et al. 2018), and the data of RXJ0821+0752 are poorly calibrated because of an issue of water vapor radiometer (Vantghem et al. 2017). Thus, we did not include them in our sample. The list of the 9 remaining galaxies are shown in table 1. We call the central galaxies by the names of their host clusters. The galaxy redshifts  $z$  are those determined by optical observations.

The galaxies were observed with ALMA at frequencies corresponding to the CO(1-0), CO(2-1), or CO(3-2) rotational transition lines as well as at additional spectral windows that were used to image the mm/submm ( $\sim 100\text{--}300 \text{ GHz}$ ) continuum emission. The observations were single pointing ones centered on the AGNs, and they were calibrated using the appropriate version of Common Astronomy Software Application (CASA) software (McMullin et al. 2007) and ALMA Pipeline used for the quality assurance. Data sets taken in the early ALMA Cycles were calibrated by the EA ALMA Regional Center (EA-ARC) through the request via the ALMA Helpdesk because of unavailability of the recommended CASA version. We confirmed that maximum recoverable scales are much larger than 500 pc for all the targets.

The line and underlying continuum emissions were reconstructed using the CASA `tclean` task down to  $3\sigma$  level. To study the line emissions, we subtracted the continuum using line-free channels with the CASA task `uvcontsub` (fitorder=1). Following previous studies (Olivares et al. 2019; Russell et al. 2019), we adopted Briggs weighting with a robust parameter of 2 (natural weighting). Each receiver was tuned to cover one of the abovementioned lines. The targets were observed with four spectral windows except for 2A0335+096 and PKS 0745-191 (two windows). Each spectral window has a bandwidth of 1.875 or 2.0 GHz. The synthesized beam size, and rms in each final datacube are shown in table 1.

## 3 Results

Using the CASA task `immoments`, images of the integrated intensity, velocity center, and full width at half-maximum (FWHM) were created for the vicinities of the AGNs in the 9 galaxies covering each CO line (figure 1). We extracted spectra from the central 500 pc region centered on the AGNs. Each spectrum was fitted with a model

**Table 1.** Target and observation details.

Target	$z^*$	CO line	ALMA ID project	Obs. time (min)	Date	Beam ( $''$ )	PA (deg)	$v$ binning ( $\text{km s}^{-1}$ )	rms ( $\text{mJy bm}^{-1}$ )
NGC 5044	0.00928 <sup>a</sup>	J=2-1	2011.0.00735.S	28	2012-01-13	$2.114 \times 1.242$	-32.517	20	1.4
Centaurus	0.0099 <sup>b</sup>	J=1-0	2015.1.01198.S	78	2016-01-27	$2.315 \times 1.765$	76.464	30	0.3
Abell 262	0.01619 <sup>c</sup>	J=2-1	2015.1.00598.S	11	2016-06-27	$0.954 \times 0.619$	12.363	20	0.6
Abell 3581	0.0218 <sup>c</sup>	J=2-1	2015.1.00644.S	87	2016-05-03	$0.687 \times 0.590$	-76.863	20	0.3
Abell 2052	0.0345 <sup>d</sup>	J=2-1	2015.1.00627.S	80	2016-08-11	$0.325 \times 0.270$	-40.989	20	0.3
2A0335+096	0.03458 <sup>e</sup>	J=1-0	2012.1.00837.S	71	2014-07-22	$1.322 \times 1.074$	-26.407	20	0.5
Hydra A	0.05435 <sup>f</sup>	J=2-1	2016.1.01214.S	45	2016-10-23	$0.243 \times 0.173$	88.838	10	0.4
Abell 1795	0.06331 <sup>d</sup>	J=2-1	2015.1.00623.S	70	2016-06-11	$0.811 \times 0.609$	-14.849	20	0.4
PKS 0745-191	0.1028 <sup>c</sup>	J=3-2	2012.1.00837.S	25	2014-08-19	$0.274 \times 0.191$	78.452	20	0.8

\* References of redshifts: (a) Ogando et al. (2008), (b) Fouque et al. (1992), (c) Olivares et al. (2019), (d) Albareti et al. (2017), (e) Zaw et al. (2019), and (f) Rose et al. (2019).

consisting of one or two Gaussian components (figure 2). The significance levels of those line components are  $> 5\sigma$ . The best-fitting line center velocity  $v$  relative to the galaxy rest frame, FWHM, and integrated intensity for each gaussian component  $S_{\text{CO}}\Delta v$  are presented in table 2. We ignored line-like structures if the line center velocity is  $|v| \gtrsim 500 \text{ km s}^{-1}$  because the corresponding gases are unlikely to be bound to the nuclei; they may be gas blobs that are falling toward or being ejected from the galactic centers. Hydra A has a prominent disk and substantial absorption due to the disk is seen at the line frequency at the position of the AGN (Rose et al. 2019; see figure 1). Thus, we excluded the innermost 160 pc, and we extracted and examined the spectra in the eastern and western regions of the AGN separately (figure 2). The parenthesized FWHM values shown in table 2 are the flux averages of the two gaussian components except for Hydra A, for which it is the flux average of the east and west values.

### 3.1 Molecular gas mass

From the CO intensities  $S_{\text{CO}}\Delta v$  presented in table 2, we derive the masses of molecular gas within 500 pc from the AGNs using the following relation from Bolatto et al. (2013):

$$M_{\text{mol}} = \frac{1.05 \times 10^4}{F_{\text{ul}}} \left( \frac{X_{\text{CO}}}{2 \times 10^{20} \frac{\text{cm}^{-2}}{\text{K km s}^{-1}}} \right) \times \left( \frac{1}{1+z} \right) \left( \frac{S_{\text{CO}}\Delta v}{\text{Jy km s}^{-1}} \right) \left( \frac{D_L}{\text{Mpc}} \right)^2 M_{\odot}, \quad (1)$$

where  $X_{\text{CO}}$  is the CO-to- $\text{H}_2$  conversion factor,  $D_L$  is the luminosity distance, and  $F_{\text{ul}}$  is the factor that represents an approximate conversion between the expected flux density ratios of two lines, where  $u$  and  $l$  represent the upper and lower levels, respectively. For CO(1-0),  $F_{10} = 1$ , and for CO(2-1) and CO(3-2) the values are  $F_{21} = 3.2$  and  $F_{32} = 7.2$ , respectively (Rose et al. 2019; Russell

et al. 2019). The conversion factor  $X_{\text{CO}}$  is not well-understood for elliptical galaxies. Thus, we adopt a standard value of  $X_{\text{CO}} = 2 \times 10^{20} \text{ cm}^{-2} (\text{K km s}^{-1})^{-1}$  measured in the Milky Way, following previous studies (Olivares et al. 2019; Russell et al. 2019 and see their discussion). The results are shown in table 3. When there are two gaussian components in the spectrum, the mass is their summation.

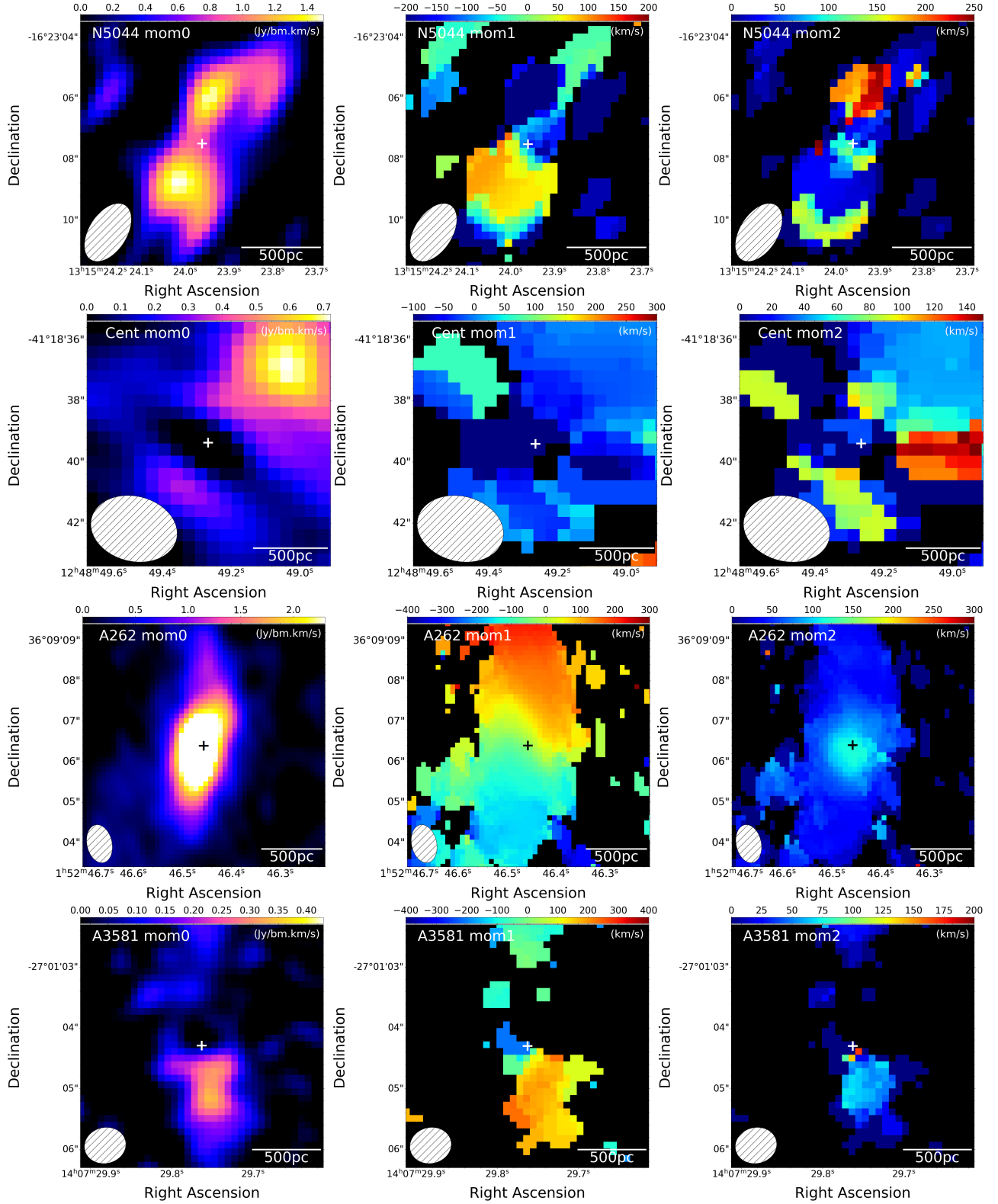
### 3.2 Circumnuclear gas and jet power

Figure 3 shows the relation between the molecular gas mass at  $r < 500 \text{ pc}$  ( $M_{\text{mol}}$ ) and the jet power required to inflate X-ray cavities ( $P_{\text{cav}}$ ). The data of  $P_{\text{cav}}$  have been taken from the literature (Rafferty et al. 2006; Pulido et al. 2018). A correlation can be seen between  $M_{\text{mol}}$  and  $P_{\text{cav}}$ , and the Pearson correlation coefficient on the logarithmic scales is 0.754 with  $p$ -value 0.019. The correlation can be described by a power-law model of the form:

$$\log \left( \frac{P_{\text{cav}}}{10^{42} \text{ erg s}^{-1}} \right) = A_1 \log \left( \frac{M_{\text{mol}}}{M_{\odot}} \right) + B_1. \quad (2)$$

Using the BCES ( $Y|X$ ) estimator (Akritas & Bershady 1996), which accounts for errors in both axes and the presence of possible intrinsic scatter, we obtain  $A_1 = 1.3 \pm 0.4$  and  $B_1 = -8.6 \pm 3.0$ . In other words, the correlation indicates that the jet power is promotional to the average density of the circumnuclear molecular gas because we considered the mass within the fixed radius and  $A_1 \sim 1$ . Abell 262 appears to be an outlier of this correlation because it is outside the  $3\sigma$  confidence range (figure 3). If we exclude Abell 262 from the sample, the correlation coefficient increases to 0.906 with  $p$ -value 0.0020. Abell 262 has a lower AGN activity despite retaining a large amount of gas. Possible reasons will be discussed in section 4.1.

The gas accretion rate  $\dot{M}$  may be more directly related to the AGN activity than  $M_{\text{mol}}$ . The accretion is likely to be induced by the angular momentum transfer by turbulence (Pizzolato & Soker 2010; Gaspari et al. 2017). In



**Fig. 1.** From left to right, close-up CO integrated intensity (moment 0) map, velocity distribution (moment 1) map of the  $\geq 3\sigma$  CO emission, and velocity dispersion (moment 2) map of the  $\geq 3\sigma$  CO emission. The AGNs are located at the center of the figures. The beam is plotted in white at the bottom left side of each panel. Note that the maps for Abell 2052 appear to be different from those provided by Russell et al. (2019). This is may be because of the difference of beam sizes.

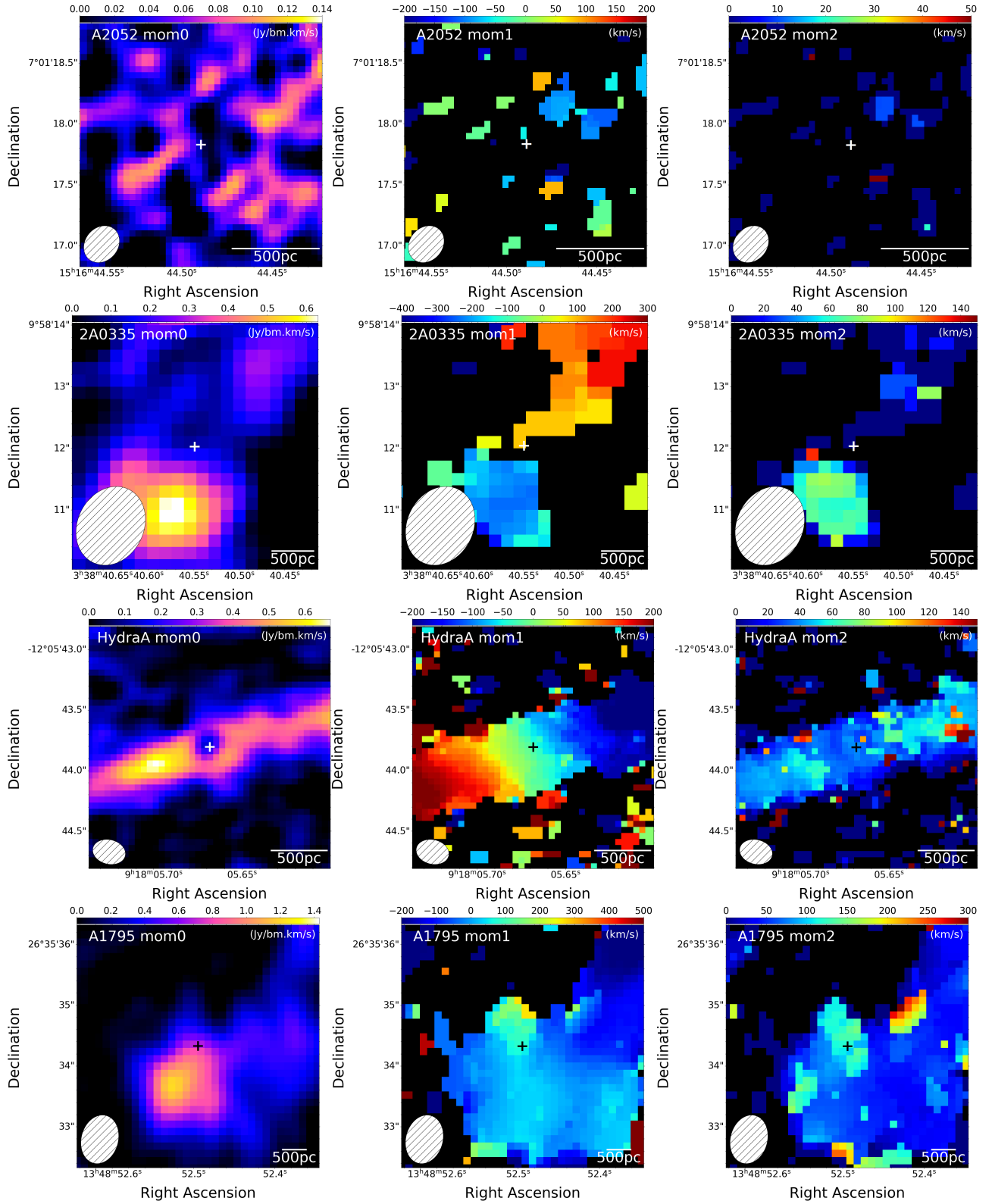


Fig. 1. Continued

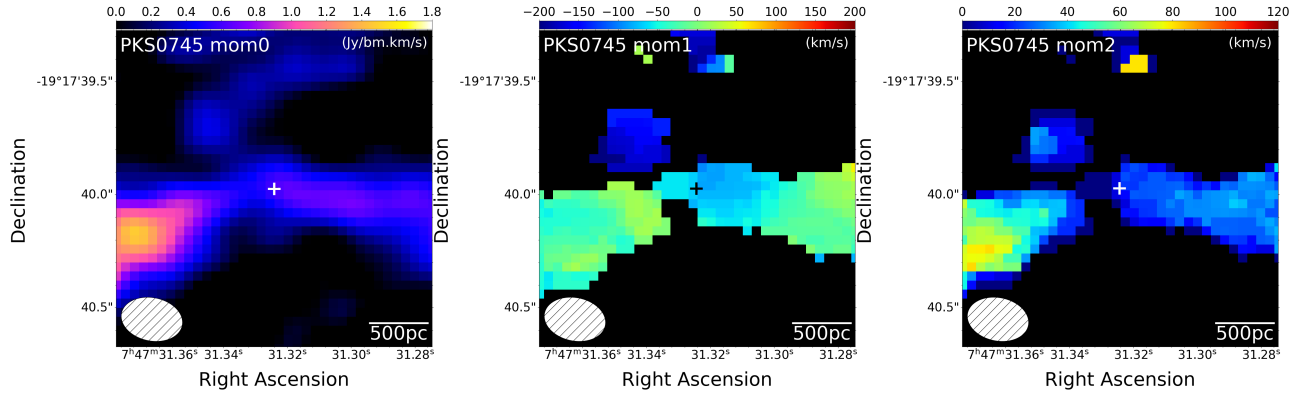


Fig. 1. Continued

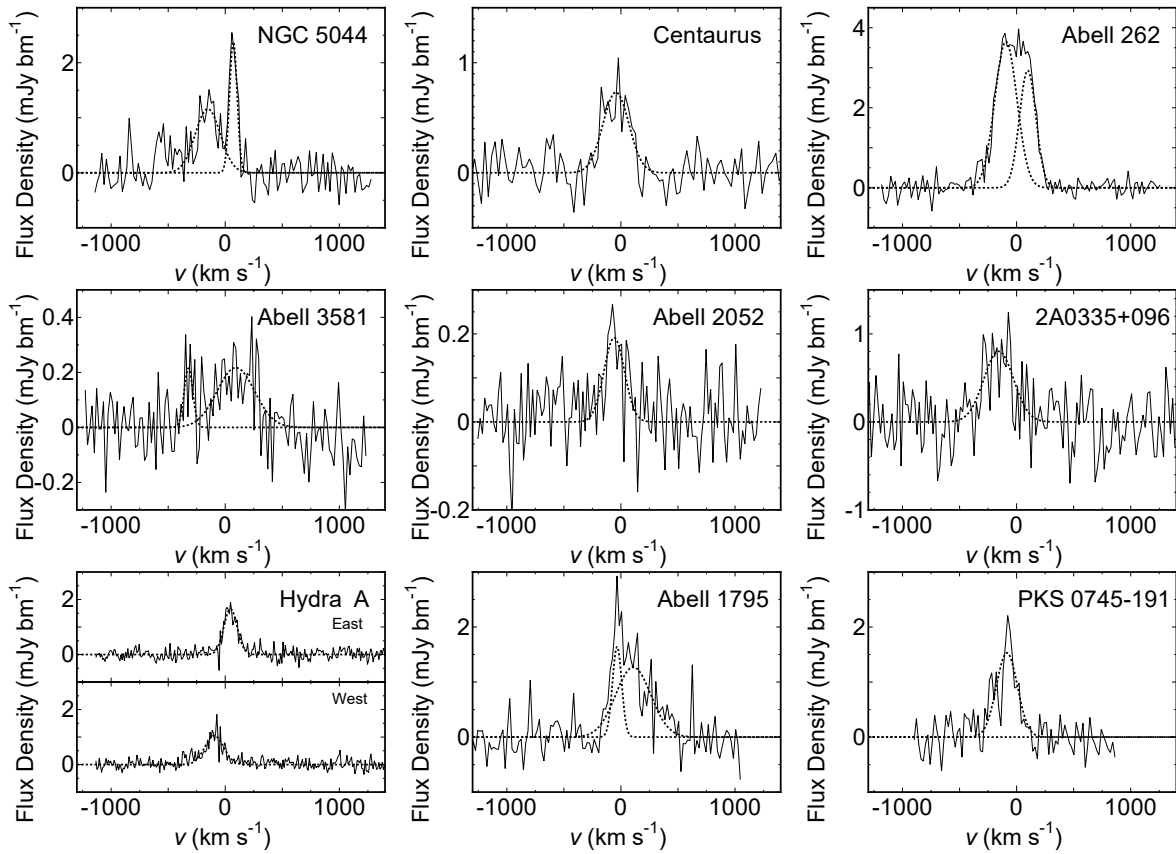


Fig. 2. CO line spectrum within 500 pc from the AGNs. The dotted lines show the best-fit gaussian components.

**Table 2.** Observed CO and mm/submm continuum emissions.

Target	$v$ (km s <sup>-1</sup> )	FWHM* (km s <sup>-1</sup> )	$S_{\text{CO}}\Delta v$ (mJy bm <sup>-1</sup> km s <sup>-1</sup> )	$\nu_{\text{con}}$ (GHz)	$F_{\text{con}}$ (mJy)	$\alpha_{\text{CO}}$	$\Delta\nu_{\text{ul}}^\dagger$ (GHz)
NGC 5044	70.8 ± 3.9	77.7 ± 9.9	197 ± 32	235.2	49.5 ± 3.7	0.22 ± 2.46	15.3
	-153 ± 16	259 ± 42 (190 ± 34)	320 ± 63				
Centaurus	-44 ± 15	268 ± 36	208 ± 37	107.1	51.6 ± 2.6	-1.30 ± 0.49	11.9
Abell 262	96.9 ± 9.1	170 ± 14	529 ± 67	235.6	3.336 ± 0.069	-0.76 ± 1.13	15.8
	-94 ± 11	229 ± 18 (207 ± 17)	890 ± 76				
Abell 3581	-322 ± 15	90 ± 36	21 ± 11	231.8	107.5 ± 3.7	-0.22 ± 0.77	14.0
	93 ± 31	388 ± 76 (332 ± 70)	90 ± 23				
Abell 2052	-59 ± 17	211 ± 41	43 ± 11	229.5	34.3 ± 3.1	-1.08 ± 1.29	15.0
2A0335+096	-157 ± 24	307 ± 56	262 ± 63	110.5	6.01 ± 0.34	0.38 ± 4.40	2.0
Hydra A	-96.8 ± 5.6	194 ± 13	217 ± 20	227.6	65.23 ± 0.19	-0.749 ± 0.062	16.0
	46.0 ± 3.0	137.7 ± 7.1 (164 ± 10)	243 ± 16				
Abell 1795	-33.7 ± 6.8	95 ± 20	166 ± 46	225.8	3.29 ± 0.041	-2.06 ± 0.41	15.6
	108 ± 27	362 ± 44 (294 ± 39)	488 ± 81				
PKS 0745-191	-85.2 ± 9.7	217 ± 23	353 ± 49	314.6	5.03 ± 0.35	11.6 ± 14.5	1.9

\* Flux-averaged ones are parenthesized.

† Frequency difference between upper and lower frequency windows.

**Table 3.** Molecular gas mass and mm/submm continuum luminosity obtained in this study.

Target	$M_{\text{mol}}$ (10 <sup>7</sup> M <sub>⊙</sub> )	$t_{\text{acc}}$ (10 <sup>7</sup> yr)	$\dot{M}$ (M <sub>⊙</sub> yr <sup>-1</sup> )	$L_{\text{con}}$ (10 <sup>42</sup> erg s <sup>-1</sup> )
NGC 5044	2.0 ± 0.2	4.0	0.48 ± 0.13	(9.2 ± 0.7) × 10 <sup>-3</sup>
Centaurus	1.1 ± 0.2	2.9	0.38 ± 0.12	(1.3 ± 0.1) × 10 <sup>-2</sup>
Abell 262	24 ± 2	3.7	6.6 ± 1.0	(1.9 ± 0.0) × 10 <sup>-3</sup>
Abell 3581	2.9 ± 0.7	2.3	1.2 ± 0.5	0.11 ± 0.0
Abell 2052	5.4 ± 1.5	3.6	1.5 ± 0.7	(9.1 ± 0.8) × 10 <sup>-2</sup>
2A0335+096	6.1 ± 1.5	2.5	2.4 ± 1.0	(2.1 ± 0.1) × 10 <sup>-2</sup>
Hydra A	42 ± 2	4.7	8.9 ± 1.0	0.44 ± 0.0
Abell 1795	15 ± 2	2.6	5.8 ± 2.0	(3.1 ± 0.0) × 10 <sup>-2</sup>
PKS 0745-191	39 ± 5	3.5	11 ± 3	0.12 ± 0.01

**Table 4.** Properties of the targets.

Target	$P_{\text{cav}}^*$ (10 <sup>42</sup> erg s <sup>-1</sup> )	$F_{1.4}^\dagger$ (mJy)	$L_{1.4}$ (10 <sup>42</sup> erg s <sup>-1</sup> )	$M_{\text{BH}}^\ddagger$ (10 <sup>9</sup> M <sub>⊙</sub> )
NGC 5044	4.2 <sup>+1.2</sup> <sub>-2.0</sub>	34.7 ± 1.1	(9.3 ± 0.3) × 10 <sup>-5</sup>	0.2
Centaurus	7.4 <sup>+5.8</sup> <sub>-1.8</sub>	3980 ± 110	(1.2 ± 0.0) × 10 <sup>-2</sup>	0.4 <sup>+0.1</sup> <sub>-0.1</sub>
Abell 262	9.7 <sup>+7.5</sup> <sub>-2.6</sub>	65.7 ± 2.3	(5.4 ± 0.2) × 10 <sup>-4</sup>	0.4 <sup>+0.2</sup> <sub>-0.1</sub>
Abell 3581	3.1	645.5 ± 22.8	(9.7 ± 0.3) × 10 <sup>-3</sup>	0.4 <sup>+0.1</sup> <sub>-0.1</sub>
Abell 2052	150 <sup>+200</sup> <sub>-70</sub>	5499 ± 209	(2.1 ± 0.1) × 10 <sup>-1</sup>	0.4 <sup>+0.2</sup> <sub>-0.1</sub>
2A0335+096	24 <sup>+23</sup> <sub>-6</sub>	36.7 ± 1.8	(1.6 ± 0.1) × 10 <sup>-3</sup>	0.5 <sup>+0.3</sup> <sub>-0.2</sub>
Hydra A	430 <sup>+200</sup> <sub>-50</sub>	40850 ± 1279	4.0 ± 0.1	0.9 <sup>+0.7</sup> <sub>-0.4</sub>
Abell 1795	160 <sup>+230</sup> <sub>-50</sub>	925 ± 28	(1.2 ± 0.0) × 10 <sup>-1</sup>	0.6 <sup>+0.3</sup> <sub>-0.2</sub>
PKS 0745-191	1700 <sup>+1400</sup> <sub>-300</sub>	2372 ± 84	(8.8 ± 0.3) × 10 <sup>-1</sup>	1.1 <sup>+0.7</sup> <sub>-0.4</sub>

\* Jet power from Rafferty et al. (2006) and Pulido et al. (2018).

† 1.4 GHz flux from Condon et al. (1998) except for Centaurus (Kuehr et al. 1981)

‡ Black hole mass from Rafferty et al. (2006) except for NGC 5044 (David et al. 2009).

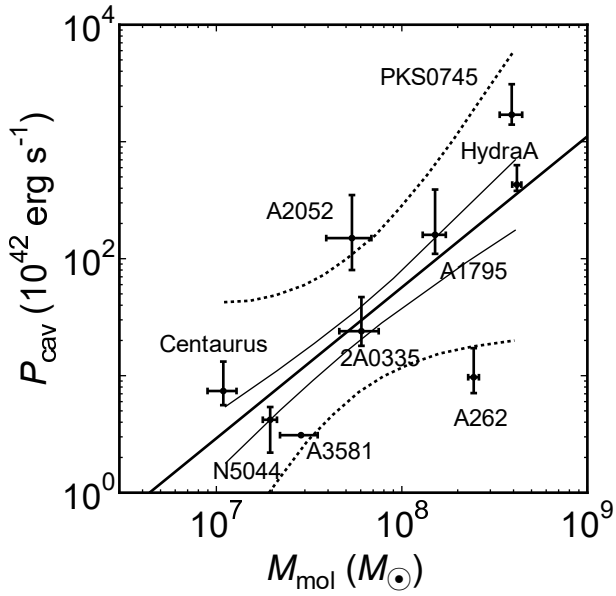


**Fig. 3.** Molecular gas mass within 500 pc from the AGN compared with the jet power estimated from the X-ray cavities. The thick solid line shows the best-fitting power-law model, determined using the BCES estimator. The thin solid and dotted lines show the  $1\sigma$  and  $3\sigma$  confidence ranges, respectively.

this case, the accretion process can be regarded as a diffusion process of gas clumps, and the diffusion coefficient is  $\nu \sim \ell_t v_t$ , where  $\ell_t$  and  $v_t$  is the eddy scale and the velocity of the turbulence, respectively. Thus, the diffusion or the accretion time scale for the gas distributed on a scale of  $r_g$  is  $t_{\text{acc}} \sim r_g^2/\nu$ , and the accretion rate is  $\dot{M} \sim M_{\text{mol}}/t_{\text{acc}}$ . We note that this estimation can even be applied to the standard disk (Shakura & Sunyaev 1973). Since the kinetic viscosity coefficient can be regarded as the diffusion coefficient, the accretion time of a disk on a scale of  $r_g$  is also  $t_{\text{acc}} \sim r_g^2/\nu$  (section 6 of Pringle 1981). Thus, we adopt the relation of  $\dot{M} = M_{\text{mol}}/t_{\text{acc}}$  regardless of whether molecular gas has a disk-like structure or not. We assume that  $v_t = \text{FWHM}/(2\sqrt{2\ln 2}) \approx \text{FWHM}/2.35$  and  $\ell_t = \alpha r_g$ , where  $r_g = 500$  pc and  $\alpha = 0.15$  (Shapiro & Teukolsky 1983). For the FWHM, we use the flux averaged values when there are two gaussian components (parenthesized ones in table 3). We note that the derived  $v_t$  may include a rotational component on a small scale that cannot be spatially resolved (see Nagai et al. 2019) and it should be regarded as the upper limit. Moreover, not all the in-flowing gas ( $\dot{M}$ ) is eventually swallowed by the black hole because some of it is consumed in star formation (Fujita et al. 2022). The obtained  $t_{\text{acc}}$  and  $\dot{M}$  are shown in table 3.

Figure 4 shows the relation between  $\dot{M}$  and  $P_{\text{cav}}$ , which is similar to that between  $M_{\text{mol}}$  and  $P_{\text{cav}}$  (figure 3). The correlation coefficient is 0.733 with  $p$ -value 0.025, and it is 0.871 with  $p$ -value 0.0049 if we exclude Abell 262 because

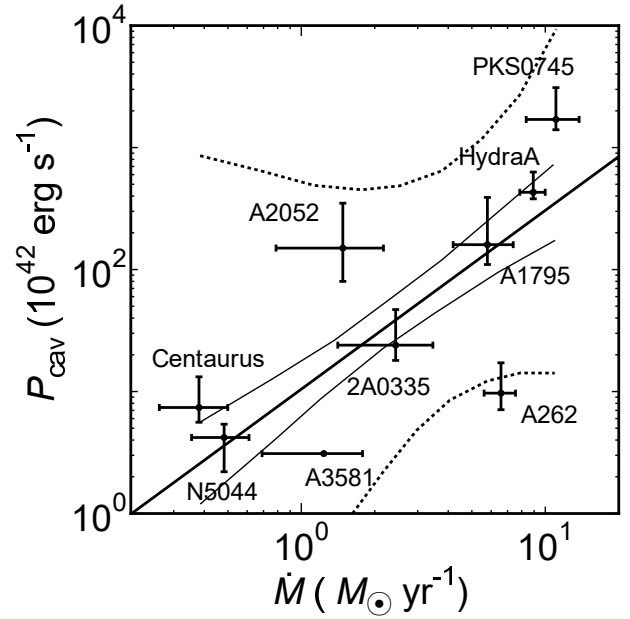


**Fig. 4.** Same as figure 3 but the gas accretion rate compared with the jet power estimated from X-ray cavity observations.

it is almost at the end of the  $3\sigma$  confidence range. The correlation among the 9 objects can be represented by a power-law model of the form:

$$\log \left( \frac{P_{\text{cav}}}{10^{42} \text{ erg s}^{-1}} \right) = A_2 \log \left( \frac{\dot{M}}{M_{\odot} \text{ yr}^{-1}} \right) + B_2. \quad (3)$$

The BCES ( $Y|X$ ) estimator gives  $A_2 = 1.5 \pm 0.6$  and  $B_2 = 1.0 \pm 0.3$ . The similarity between figures 3 and 4 reflects the fact that while FWHM varies only a factor of few,  $M_{\text{mol}}$  ranges nearly two orders of magnitude. This suggests that the mass of circumnuclear molecular gas is the main factor that determines the jet activity. Thus, the  $\dot{M}$ - $P_{\text{cav}}$  relation seems to be robust even if we consider potential uncertainties such as the gas morphology (disk-like or not) and the contamination of a rotational velocity component.

### 3.3 Circumnuclear gas and continuum emission

Since radio continuum emission is observed as a point source at the position of the AGNs, it should come from the vicinity of the AGNs ( $\lesssim 500$  pc) and reflect their recent activity. We derive the continuum flux at line-free channels.

We convert fluxes at observed frequencies to those at the rest-frame CO(1-0) line frequency ( $\nu_{10} = 115.3$  GHz) assuming that the continuum emission is represented by a power-law  $S_{\nu} \propto (\nu/\nu_{10})^{\beta}$ , where  $\nu$  is the frequency. We adopt a typical spectral index of  $\beta = -0.75$ . For an object at the redshift  $z$  and observed at the frequency  $\nu_{\text{con}}$ , the radio continuum luminosity at the frequency  $\nu_{10}$  is estimated

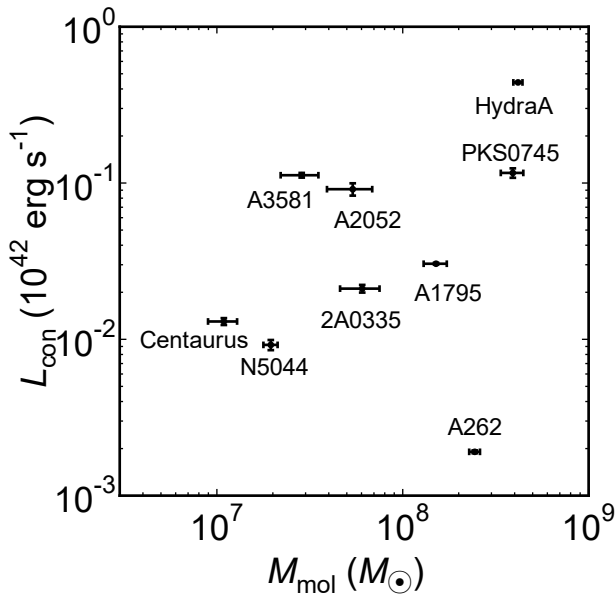


Fig. 5. Continuum luminosity in the mm/submm band compared with the molecular gas mass within 500 pc from the AGN.

to be

$$L_{\text{con}} = \frac{4\pi D_L^2 \nu_{\text{con}} F_{\text{con}}}{[(1+z)\eta]^{1+\beta}}, \quad (4)$$

where  $F_{\text{con}}$  is the observed flux (mJy) and  $\eta$  is the line frequency ratios ( $\eta = 1$  for CO(1-0),  $\eta \approx 2$  for CO(2-1)<sup>1</sup>, and  $\eta \approx 3$  for CO(3-2)), which is required for the flux conversion among different line frequencies. The derived luminosities  $L_{\text{con}}$  are presented in table 3 and they are compared with  $M_{\text{mol}}$  in figure 5. The correlation coefficient is 0.295 and the  $p$ -value is 0.44, which is much larger than the conventional threshold of 0.05. Thus, it is unlikely that that  $L_{\text{con}}$  is correlated with  $M_{\text{mol}}$ . Again, Abell 262 appears to be an outlier because the radio luminosity is extremely small for its large  $M_{\text{mol}}$ . If we exclude Abell 262 from the sample, the coefficient is 0.713 with  $p$ -value 0.047, which shows a sign of correlation.

Traditionally, radio emissions at lower frequencies have been used as an indicator of AGN activities (Bîrzan et al. 2004; Pulido et al. 2018). Figure 6 compares the radio luminosity estimated from 1.4 GHz observations (NRAO/VLA Sky Survey; Condon et al. 1998) with the mass of the circumnuclear molecular gas ( $M_{\text{mol}}$ ). The former is derived by

$$L_{1.4} = \frac{4\pi D_L^2 \nu_{1.4} F_{1.4}}{(1+z)^{1+\beta}}, \quad (5)$$

where  $\nu_{1.4}$  is 1.4 GHz,  $F_{1.4}$  is the observed flux at 1.4 GHz, and  $\beta = -0.75$ . Since our targets are at lower redshifts

<sup>1</sup> Exactly speaking, the continuum flux is not measured right at the frequency of the CO line. However, since the index is  $1 + \beta = 0.35$ , the minor modification  $\eta$  does not affect the results.

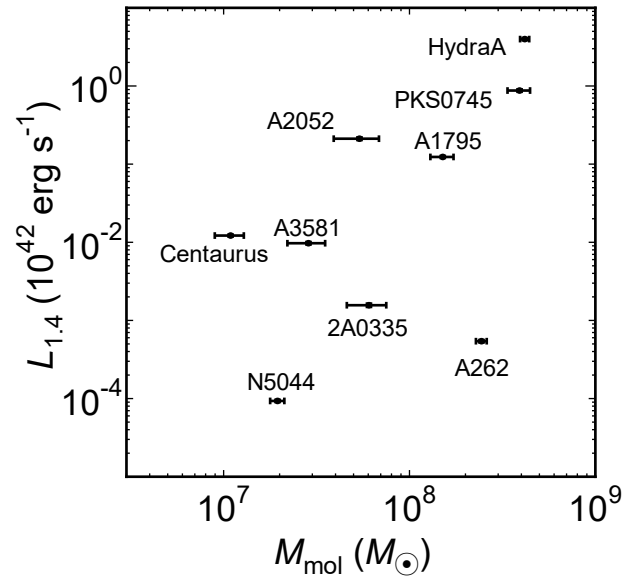


Fig. 6. Continuum luminosity at 1.4 GHz compared with the molecular gas mass within 500 pc from the AGN.

( $z \lesssim 0.1$ ), the correction of  $(1+z)^{1+\beta}$  is insensitive to  $\beta$ . The correlation coefficient is 0.556 with  $p$ -value 0.12. Thus,  $L_{1.4}$  is unlikely to be correlated with  $M_{\text{mol}}$ . However, if Abell 262 is ignored, the correlation coefficient is 0.778 with  $p$ -value 0.023, which may indicate the existence of correlation.

## 4 Discussion

### 4.1 Circumnuclear gas and AGN activity

We have shown that the mass of circumnuclear molecular gas ( $M_{\text{mol}}$ ) within a fixed radius (500 pc) has a correlation with the jet power estimated from X-ray cavities ( $P_{\text{cav}}$ ; figure 3). This suggests that the circumnuclear molecular gas serves as the fuel for AGN feedback (Fujita et al. 2022). Assuming that the gas accretion is caused by angular momentum transport by turbulence, the accretion rate ( $\dot{M}$ ) is also correlated with  $P_{\text{cav}}$  (figure 4), although the  $\dot{M}$ - $P_{\text{cav}}$  relation is virtually the  $M_{\text{mol}}$ - $P_{\text{cav}}$  relation. We conclude that the jet power depends on the average density of the circumnuclear molecular gas because we considered the mass within the fixed radius. Since  $A_1 = 1.3 \pm 0.4$  in equation (2), a simple relation of  $P_{\text{cav}} \propto M_{\text{mol}}$  is acceptable. This fact would be useful when constructing sub-grid models of AGN feedback in numerical simulations, which have often adopted the classical Bondi accretion rate. The correlation between the mass of circumnuclear molecular gas and the AGN activity has been known for disk galaxies (e.g. Izumi et al. 2016). Thus, the AGN fueling mechanism for elliptical galaxies may be similar to that in the

disk galaxies.

In contrast with  $P_{\text{cav}}$ , the continuum luminosities both at  $\sim 1.4$  GHz ( $L_{1.4}$ ) and  $\sim 100$ – $300$  GHz ( $L_{\text{con}}$ ) seem to have no correlation with  $M_{\text{mol}}$  (figures 5 and 6). The difference may be ascribed to the relevant time scales of AGN activities. The jet power  $P_{\text{cav}}$  is often described by the ratio of the energy required to inflate the cavity to its evolution time ( $t_{\text{cav}}$ ) such as the cavity’s buoyancy age (Allen et al. 2006; Rafferty et al. 2006; see also Fujita et al. 2016). Thus,  $P_{\text{cav}}$  reflects the AGN activity averaged over on a time scale of  $t_{\text{cav}}$ , which is estimated to be  $\sim 10^7$  yr (Rafferty et al. 2006). Interestingly, it is comparable to the gas accretion time  $t_{\text{acc}}$  (table 3). On the other hand, since the mm/submm ( $\sim 100$ – $300$  GHz) continuum is observed as nuclear point sources coincident with the AGNs, the size of the emitting regions should be  $\lesssim 500$  pc. Since the light-travel time of the regions is only  $\lesssim 1600$  yr, the emission virtually reflects the current activity of the AGN. The existence of the correlation between  $P_{\text{cav}}$  and  $M_{\text{mol}}$  and the non-existence between the continuum luminosities and  $M_{\text{mol}}$  suggest that the circumnuclear gas is rather persistently fueling the AGN activity on a longer time scale ( $t_{\text{cav}} \sim 10^7$  yr). However, since  $L_{1.4}$  is the total luminosity of the galaxy, it may include emissions from larger and older structures such as  $\sim$  kpc radio jets and lobes. Thus, it could be proved that  $L_{1.4}$  is more correlated with  $M_{\text{mol}}$  than  $L_{\text{con}}$  with more samples.

In figures 3–6, Abell 262 appears to be an outlier. While it has a large amount of circumnuclear molecular gas ( $M_{\text{mol}}$ ), both the jet power ( $P_{\text{cav}}$ ) and the mm/submm continuum luminosities ( $L_{\text{con}}$  and  $L_{1.4}$ ) are small. This might be explained if the AGN activity has been gentle for a long time. Thus, there may be an additional factor that affects the activity other than the mass of circumnuclear molecular gas. For example, compared with other galaxies with similar amount of  $M_{\text{mol}}$  (Abell 1795, Hydra A, and PKS 0745–191), the mass of the black hole ( $M_{\text{BH}}$ ) at the center of Abell 262 is small (table 4). This may lead to a lower efficiency of power generation, which may explain its peculiarity. Alternatively, the AGN may have been at a “pre-feedback” phase (Ubertosi et al. 2023).

#### 4.2 The origin of the mm/submm continuum emission

So far, the origin of the continuum emission from the AGNs in massive elliptical galaxies has not been much studied in the mm/submm band. We study the spectral index of the continuum emission  $\beta_{\text{CO}}$  by comparing the fluxes between the upper and lower sidebands of the CO lines. For most galaxies, the frequency difference between the side-

bands is  $\Delta\nu_{\text{ul}} \sim 15$  GHz (table 2). However, it is only  $\sim 2$  GHz for 2A0335+096 and PKS0745–191, and their indices cannot be well constrained. Table 2 presents the results. Except for 2A0335+096 and PKS0745–191, the indices are  $\beta_{\text{CO}} \lesssim 0$ , which indicates that the emission is likely to be dominated by synchrotron radiation and the contribution of dust emission is minor. Thus, the assumption of  $\beta = -0.75$  in section 3.3 seems to be reasonable.

Figure 7 compares the continuum luminosities at  $\nu \sim \nu_{10} = 115.3$  GHz ( $L_{\text{con}}$ ) with those at 1.4 GHz ( $L_{1.4}$ ) estimated in section 3.3. Those two luminosities are positively correlated and the correlation coefficient is 0.823 with  $p$ -value 0.0059. The correlation among the 9 objects can be represented by a power-law model of the form:

$$\log\left(\frac{L_{\text{con}}}{10^{42}\text{erg s}^{-1}}\right) = A_3 \log\left(\frac{L_{1.4}}{10^{42}\text{erg s}^{-1}}\right) + B_3. \quad (6)$$

The BCES ( $Y|X$ ) estimator gives  $A_3 = 0.39 \pm 0.09$  and  $B_3 = -1.6 \pm 0.1$ . We have confirmed that there is no correlation between fluxes  $F_{\text{con}}$  and  $F_{1.4}$  (the correlation coefficient is -0.2567 and  $p$ -value is 0.48). Thus, it is unlikely that the  $L_{1.4}$ – $L_{\text{con}}$  relation with  $A_3 \neq 1$  is due to redshift selection effects (Feigelson & Berg 1983). The fact that  $A_3$  is significantly smaller one means that the ratio  $L_{\text{con}}/L_{1.4} \propto L_{1.4}^{A_3-1}$  increases as  $L_{1.4}$  decreases. This suggests that the mm/submm continuum emission from the AGNs with large  $L_{1.4}$  is pure synchrotron radiation, while that from the AGNs with smaller  $L_{1.4}$  is contaminated by additional dust emission. For the latter, the dust surrounding the AGNs may not have been destroyed because the radiation from the AGNs is less powerful.

## 5 Conclusion

We have studied the relation between the circumnuclear molecular gas and the activities of the AGNs in the massive elliptical galaxies at the center of galaxy clusters. We analyzed ALMA archival data for 9 galaxies and obtained the circumnuclear molecular gas mass at  $r < 500$  pc from the AGNs. We found that the mass has a correlation with the jet power of the AGNs. More specifically, the jet power is proportional to the average density of the circumnuclear molecular gas. Since the jet power is estimated from the size of X-ray cavities, it should be the average power over the cavity formation period. Thus, the correlation indicates that the circumnuclear gas is responsible for long-term AGN activities ( $\sim 10^7$  yr). We also estimated the mass accretion rate of the cold gas assuming that the angular momentum transfer is caused by turbulence. We showed that the accretion rate is also correlated with the jet power. On the other hand, radio continuum emissions

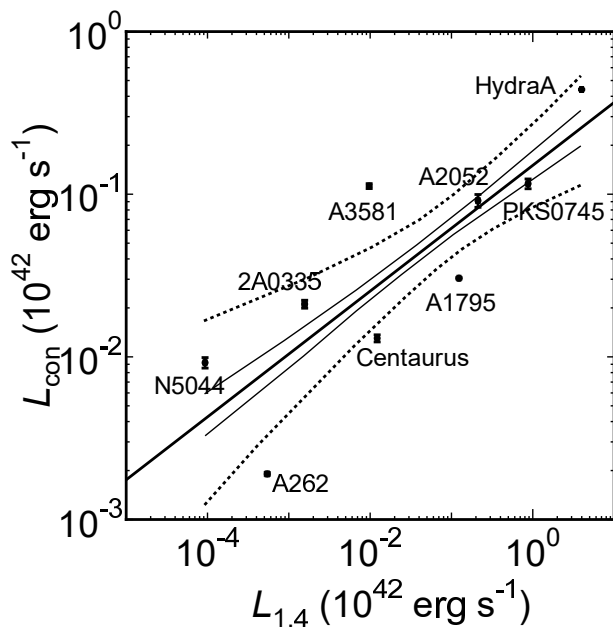


**Fig. 7.** The luminosity ( $L_{\text{con}}$ ) in the mm/submm band compared with that at 1.4 GHz ( $L_{1.4}$ ). The thick solid line shows the best-fitting power-law model that is determined using the BCES estimator. The thin solid and dotted lines show the  $1\sigma$  and  $3\sigma$  confidence ranges, respectively.

from the AGNs at 1.4 GHz and  $\sim 100$ – $300$  GHz are not correlated with the mass of circumnuclear molecular gas. This means that the gas is not directly associated with the current AGN activity. The spectra of the mm/submm ( $\sim 100$ – $300$  GHz) continuum emission indicate that they are mostly synchrotron radiation. However, comparison with 1.4 GHz luminosity suggests that dust emission is contaminated for lower luminosity AGNs, because their power may not be strong enough to destroy dust in their vicinity.

## Acknowledgments

We thank the EA ALMA Regional Center (EA-ARC) for their support. This work was supported by NAOJ ALMA Scientific Research Grant Code 2022-21A, and JSPS KAKENHI No. 20H00181, 22H01268, 22H00158 (Y.F.), 20K14531, 21H04496 (T.I.), 19K03918 (N.K.), 21H01137, 18K03709 (H.N.). This paper makes use of the following ALMA data: ADS/JAO.2011.0.00735.S, ADS/JAO.2012.1.00837.S, ADS/JAO.2012.1.00837.S, ADS/JAO.2015.1.00598.S, ADS/JAO.2015.1.00623.S, ADS/JAO.2015.1.00627.S, ADS/JAO.2015.1.00644.S, ADS/JAO.2015.1.01198.S, ADS/JAO.2016.1.01214.S. ALMA is a partnership of ESO (representing its member states), NSF (USA) and NINS (Japan), together with NRC (Canada), MOST and ASIAA (Taiwan), and KASI (Republic of Korea), in cooperation with the Republic of Chile. The Joint ALMA Observatory is operated by ESO, AUI/NRAO and NAOJ. Data analysis was in part carried out on the Multi-wavelength Data Analysis

System operated by the Astronomy Data Center (ADC), National Astronomical Observatory of Japan.

## References

- Albareti, F. D., Allende Prieto, C., Almeida, A., et al. 2017, *ApJS*, 233, 25. doi:10.3847/1538-4365/aa8992
- Allen, S. W., Dunn, R. J. H., Fabian, A. C., et al. 2006, *MNRAS*, 372, 21. doi:10.1111/j.1365-2966.2006.10778.x
- Akritis, M. G. & Bershad, M. A. 1996, *ApJ*, 470, 706. doi:10.1086/177901
- Birzan, L., Rafferty, D. A., McNamara, B. R., et al. 2004, *ApJ*, 607, 800. doi:10.1086/383519
- Bolatto, A. D., Wolfire, M., & Leroy, A. K. 2013, *ARA&A*, 51, 207. doi:10.1146/annurev-astro-082812-140944
- Bondi, H. 1952, *MNRAS*, 112, 195. doi:10.1093/mnras/112.2.195
- Cavagnolo, K. W., Donahue, M., Voit, G. M., et al. 2008, *ApJL*, 683, L107. doi:10.1086/591665
- Churazov, E., Forman, W., Jones, C., et al. 2000, *A&A*, 356, 788. doi:10.48550/arXiv.astro-ph/0002375
- Condon, J. J., Cotton, W. D., Greisen, E. W., et al. 1998, *AJ*, 115, 1693. doi:10.1086/300337
- David, L. P., Jones, C., Forman, W., et al. 2009, *ApJ*, 705, 624. doi:10.1088/0004-637X/705/1/624
- Edge, A. C. 2001, *MNRAS*, 328, 762. doi:10.1046/j.1365-8711.2001.04802.x
- David, L. P., Lim, J., Forman, W., et al. 2014, *ApJ*, 792, 94. doi:10.1088/0004-637X/792/2/94
- Fabian, A. C. 1994, *ARA&A*, 32, 277. doi:10.1146/annurev.aa.32.090194.001425
- Fabian, A. C. 2012, *ARA&A*, 50, 455. doi:10.1146/annurev-astro-081811-125521
- Feigelson, E. D. & Berg, C. J. 1983, *ApJ*, 269, 400. doi:10.1086/161051
- Fouque, P., Durand, N., Bottinelli, L., Gouguenheim, L., & Paturel, G. 1992, *Catalogue of Optical Radial Velocities* (Meudon: Observatoire de Paris-Meudon), Vol. 1, 1
- Fujita, Y., Kawakatu, N., & Nagai, H. 2022, *ApJ*, 924, 24. doi:10.3847/1538-4357/ac31a6
- Fujita, Y., Kawakatu, N., & Shlosman, I. 2016, *PASJ*, 68, 26. doi:10.1093/pasj/psw012
- Gaspari, M., Temi, P., & Brighenti, F. 2017, *MNRAS*, 466, 677. doi:10.1093/mnras/stw3108
- Izumi, T., Kawakatu, N., & Kohno, K. 2016, *ApJ*, 827, 81. doi:10.3847/0004-637X/827/1/81
- Kuehr, H., Witzel, A., Pauliny-Toth, I. I. K., et al. 1981, *A&AS*, 45, 367
- Main, R. A., McNamara, B. R., Nulsen, P. E. J., et al. 2017, *MNRAS*, 464, 4360. doi:10.1093/mnras/stw2644
- McNamara, B. R. & Nulsen, P. E. J. 2007, *ARA&A*, 45, 117. doi:10.1146/annurev.astro.45.051806.110625
- McNamara, B. R., Russell, H. R., Nulsen, P. E. J., et al. 2014, *ApJ*, 785, 44. doi:10.1088/0004-637X/785/1/44
- McMullin, J. P., Waters, B., Schiebel, D., et al. 2007, *Astronomical Data Analysis Software and Systems XVI*, 376, 127

- Nagai, H., Onishi, K., Kawakatu, N., et al. 2019, *ApJ*, 883, 193.  
doi:10.3847/1538-4357/ab3e6e
- Ogando, R. L. C., Maia, M. A. G., Pellegrini, P. S., et al. 2008, *AJ*, 135, 2424. doi:10.1088/0004-6256/135/6/2424
- Olivares, V., Salome, P., Combes, F., et al. 2019, *A&A*, 631, A22. doi:10.1051/0004-6361/201935350
- Pizzolato, F. & Soker, N. 2010, *MNRAS*, 408, 961.  
doi:10.1111/j.1365-2966.2010.17156.x
- Pringle, J. E. 1981, *ARA&A*, 19, 137.  
doi:10.1146/annurev.aa.19.090181.001033
- Pulido, F. A., McNamara, B. R., Edge, A. C., et al. 2018, *ApJ*, 853, 177. doi:10.3847/1538-4357/aaa54b
- Rafferty, D. A., McNamara, B. R., & Nulsen, P. E. J. 2008, *ApJ*, 687, 899. doi:10.1086/591240
- Rafferty, D. A., McNamara, B. R., Nulsen, P. E. J., et al. 2006, *ApJ*, 652, 216. doi:10.1086/507672
- Rose, T., Edge, A. C., Combes, F., et al. 2019, *MNRAS*, 485, 229. doi:10.1093/mnras/stz406
- Russell, H. R., McNamara, B. R., Edge, A. C., et al. 2013, *MNRAS*, 432, 530. doi:10.1093/mnras/stt490
- Russell, H. R., McNamara, B. R., Fabian, A. C., et al. 2019, *MNRAS*, 490, 3025. doi:10.1093/mnras/stz2719
- Sanderson, A. J. R., Edge, A. C., & Smith, G. P. 2009, *MNRAS*, 398, 1698. doi:10.1111/j.1365-2966.2009.15214.x
- Salomé, P. & Combes, F. 2003, *A&A*, 412, 657.  
doi:10.1051/0004-6361:20031438
- Shakura, N. I. & Sunyaev, R. A. 1973, *A&A*, 24, 337
- Shapiro, S. L. & Teukolsky, S. A. 1983, *A Wiley-Interscience Publication*, New York: Wiley, 1983
- Simionescu, A., Tremblay, G., Werner, N., et al. 2018, *MNRAS*, 475, 3004. doi:10.1093/mnras/sty047
- Ubertosi, F., Gitti, M., Brighenti, F., et al. 2023, *arXiv:2303.04821*. doi:10.48550/arXiv.2303.04821
- Vantyghem, A. N., McNamara, B. R., Edge, A. C., et al. 2017, *ApJ*, 848, 101. doi:10.3847/1538-4357/aa8fd0
- Zaw, I., Chen, Y.-P., & Farrar, G. R. 2019, *ApJ*, 872, 134.  
doi:10.3847/1538-4357/aaffaf